Miniband engineering and topological phase transitions in topological-insulator–normal-insulator superlattices

G. Krizman [1,2,*] B. A. Assaf,[3] G. Bauer,[2] G. Springholz [2] L. A. de Vaulchier,[1] and Y. Guldner[1]

[1]*Laboratoire de Physique de l'Ecole normale supérieure, ENS, Université PSL, CNRS, Sorbonne Université, 24 rue Lhomond, 75005 Paris, France*

[2]*Institut für Halbleiter und Festkörperphysik, Johannes Kepler Universität, Altenberger Strasse 69, 4040 Linz, Austria*

[3]*Department of Physics, University of Notre Dame, Notre Dame, Indiana 46556, USA*

Periodic stacking of topologically trivial and nontrivial layers with opposite symmetry of the valence and conduction bands induces topological interface states that, in the strong coupling limit, hybridize both across the topological and normal insulator layers. Using band structure engineering, such superlattices (SLs) can be effectively realized using the IV–VI lead tin chalcogenides. This leads to emergent minibands with a tunable topology, as demonstrated both by theory and experiments. The topological minibands are proven by magneto-optical spectroscopy, revealing Landau level transitions both at the center and edges of the artificial SL mini-Brillouin zone. Their topological character is identified by the topological phase transitions within the minibands observed as a function of temperature. The critical temperature of this transition as well as the miniband gap and miniband width can be precisely controlled by the layer thicknesses and compositions. This witnesses the generation of a fully tunable quasi-three-dimensional topological state that provides a template for realization of magnetic Weyl semimetals and other strongly interacting topological phases.

I. INTRODUCTION

Heterostructures of quantum materials lead to new emergent states of matter beyond what is possible in their bulk form [1–6]. In the case of topological insulators (TIs), theoretical calculations have shown that Dirac, Weyl, and nodal line fermions can be artificially created by periodically stacking a TI and a normal insulator (NI) on top of each other [3,7,8]. These superlattices (SLs) have been theoretically proposed as templates for realization of magnetic Weyl semimetals [3], Weyl superconductors [9], the quantum anomalous Hall phase [8,10–13], flat band superconductivity [5], and strongly interacting topological phases [14]. Experimental realization of TI/NI SL structures, however, has posed a formidable challenge. This is mainly due to the limitations in material combinations that are topologically different but well compatible in terms of crystal structures and heteroepitaxial growth [15,16]. As a result, up to now, most of the phases have been only theoretically predicted, and only recently, experiments have started to explore these effects [17–23].

Here, we show that the IV–VI lead tin chalcogenides (Pb,Sn)(Se,Te) topological crystalline insulators (TCIs) [24–26] provide an excellent platform for the realization of artificial TI/NI SL structures. This is because their topology [26–29], anisotropy [30,31], band alignment [32,33], and crystal symmetry [34–37] can be controlled on demand by composition, temperature, strain, and/or ferroelectric phase transitions. As a result, band structure engineering of heterostructures can be easily achieved, as has been demonstrated

for midinfrared device applications [38]. In the (Pb,Sn)(Se,Te) TCIs, the nontrivial band topology arises from the band inversion between the L_6^+ and L_6^- bands appearing at sufficiently high Sn contents. This leads to the formation of Dirac cone topological surface, respectively, interface states (TISs) that are protected by crystal symmetries [23,24] rather than by time reversal symmetry, as in conventional TIs [39]. In ultrathin films and quantum wells (QWs), the interface states at the upper and lower film boundaries hybridize, which leads to a gapping of the Dirac cone [26,40,41], as experimentally demonstrated in our previous work [19].

Here, we study TCI/NI SL structures with ultrathin barriers where the TISs are not only coupled across the TI QWs but also across the NI barrier layers. Using magneto-optical Landau level spectroscopy and envelope function calculations, we demonstrate that, due to this coupling, extended topological minibands (TMBs) emerge that can be precisely controlled by growth, temperature, layer thicknesses, and compositions. The minibands are directly evidenced by observation of two sets of magneto-optical transitions occurring at the center and edge of the mini-Brillouin zone (BZ) imposed by the artificial periodicity of the SL structure. In this way, we reveal that their dispersion, gap size, and miniband width can be perfectly controlled by tuning of the coupling constants. The nontrivial miniband topology is experimentally proven by the observation of the topological phase transitions as a function of temperature used as a tuning knob for the band inversion. From our data, we construct the experimental nonmagnetic Burkov-Balents phase diagram [3] predicted for such nontrivial systems. Our results thus represent a textbook topological SL system supporting TMBs artificially designed for various device applications.
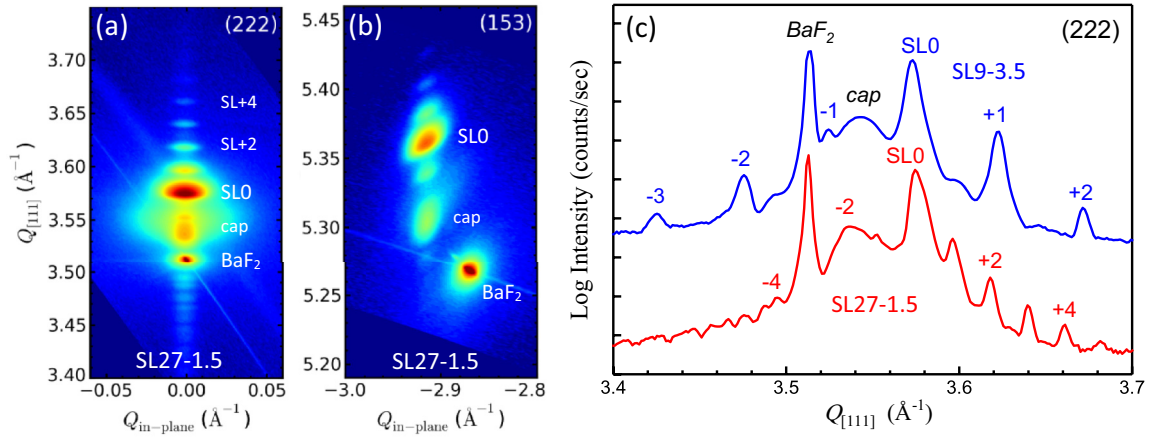
———
*gauthier.krizman@jku.at

FIG. 1. High-resolution x-ray characterization of the topological crystalline insulator (TCI)/normal insulator (NI) superlattice (SL) structures. (a) and (b) Reciprocal space maps of $Pb_{1-x}Sn_xSe/Pb_{1-y}Eu_ySn_xSe$ SLs around the symmetric (222) and asymmetric (153) Bragg reflection evidencing perfect pseudomorphic growth. (c) Radial diffraction scans along $Q_{[111]}$ normal to the surface for samples SL27-1.5 and SL9-3.5. The satellite peaks are labeled as SLx, and the diffraction peaks of the BaF_2 substrate and $Pb_{1-y}Eu_ySe$ capping layer are also indicated. The sample parameters obtained are listed in Table I.

II. GROWTH AND CHARACTERIZATION

Artificial TI/NI SL heterostructures were created by molecular beam epitaxy of nontrivial $Pb_{1-x}Sn_xSe$ TI layers (QWs) with inverted band gap, alternating with trivial NI $Pb_{1-y-x}Eu_ySn_xSe$ barrier layers. For the topologically nontrivial $Pb_{1-x}Sn_xSe$, $x_{Sn} > 0.21$ was chosen to obtain a negative gap of $2\Delta_{QW} < -20$ meV at 4 K. Alloying of europium into the barrier, on the other hand, turns the band gap positive [11], rendering $Pb_{1-y-x}Eu_ySn_xSe$ topologically trivial with a gap $2\Delta_B \sim +150$ meV for $y_{Eu} \sim 0.05$. Molecular beam epitaxy of $Pb_{1-x}Sn_xSe/Pb_{1-y}Eu_ySn_xSe$ SLs on BaF_2 (111) was carried out at a substrate temperature of 360 °C under ultrahigh vacuum conditions of 5×10^{-10} mbar using a RIBER 1000 MBE system. PbSe, SnSe, Eu, and Se effusion sources were used for growth, and a Bi_2Se_3 source for tuning of the carrier concentration to low 10^{18} cm^{-3} as determined by Hall effect measurements. The SL stacks were grown on a 50 nm $Pb_{1-y}Eu_ySe$ buffer layer predeposited on the BaF_2 substrate and a 50 nm $Pb_{1-y}Eu_ySe$ on top as a capping layer.

Perfect two-dimensional (2D) growth was achieved, evidenced by streak reflection high-energy electron diffraction patterns observed throughout SL growth. This yields perfect multilayer structures, as evidenced by high-resolution x-ray diffraction, shown in Fig. 1, showing sharp SL satellite peaks for all samples. In reciprocal space maps, shown in Figs. 1(a) and 1(b), these satellite peaks are perfectly aligned along the $Q_{[111]}$ growth direction, evidencing the very high quality of the samples and full coherency of the interfaces. The resulting SL parameters for the investigated samples are listed in Table I.

III. MODELING OF THE MINIBANDS

For proper sample design, envelope function theory [42–45] was employed to predict and model the SL band structure. The periodic SL potential shown schematically in Fig. 2(a) implies envelope functions satisfying the Bloch

theorem with a wave vector q_z that lies within the artificial SL BZ reduced within the boundaries $[-\pi/L; +\pi/L]$, determined by the SL period L. Using a 4-band $\mathbf{k} \cdot \mathbf{p}$ model, detailed in Appendix A, the TMB dispersions are calculated vs q_z, as shown in Fig. 2(b). We find that the electron and holelike states form mirrorlike minibands TMB(q_z) and TMB′(q_z), respectively. Their gaps are denoted as $2\delta_0$ and $2\delta_{\pi/L}$ at the center and boundaries of the mini-BZ, respectively. Note that, due to the multivalley band structure of the IV–VI compounds [33,46–48], the miniband dispersions are slightly different for the oblique and longitudinal valleys [solid and dashed lines in Fig. 2(b)] that are tilted, respectively, aligned parallel to the growth direction. This originates from the admixture of the

TABLE I. Sample parameters of the investigated TCI/NI SL structures composed of $Pb_{1-x}Sn_xSe$ TCI QWs alternating with trivial NI $Pb_{1-y-x}Eu_ySn_xSe$ barriers repeated N times. Also listed are the effective miniband gaps $2\delta_0$ and coupling ratios $|\tau_{QW}/\tau_B|$ [Eqs. (1a) and (1b)] for $T = 4.2$ K. $2\delta_0 < 0$ and $|\tau_{QW}/\tau_B| < 1$ indicate nontrivial topology, whereas for $2\delta_0 > 0$ and $|\tau_{QW}/\tau_B| > 1$, the SLs are topologically trivial. The well and barrier material band gaps $2\Delta_{QW}$ and $2\Delta_B$ are obtained from the fits of the magneto-optical data, which are shown later.

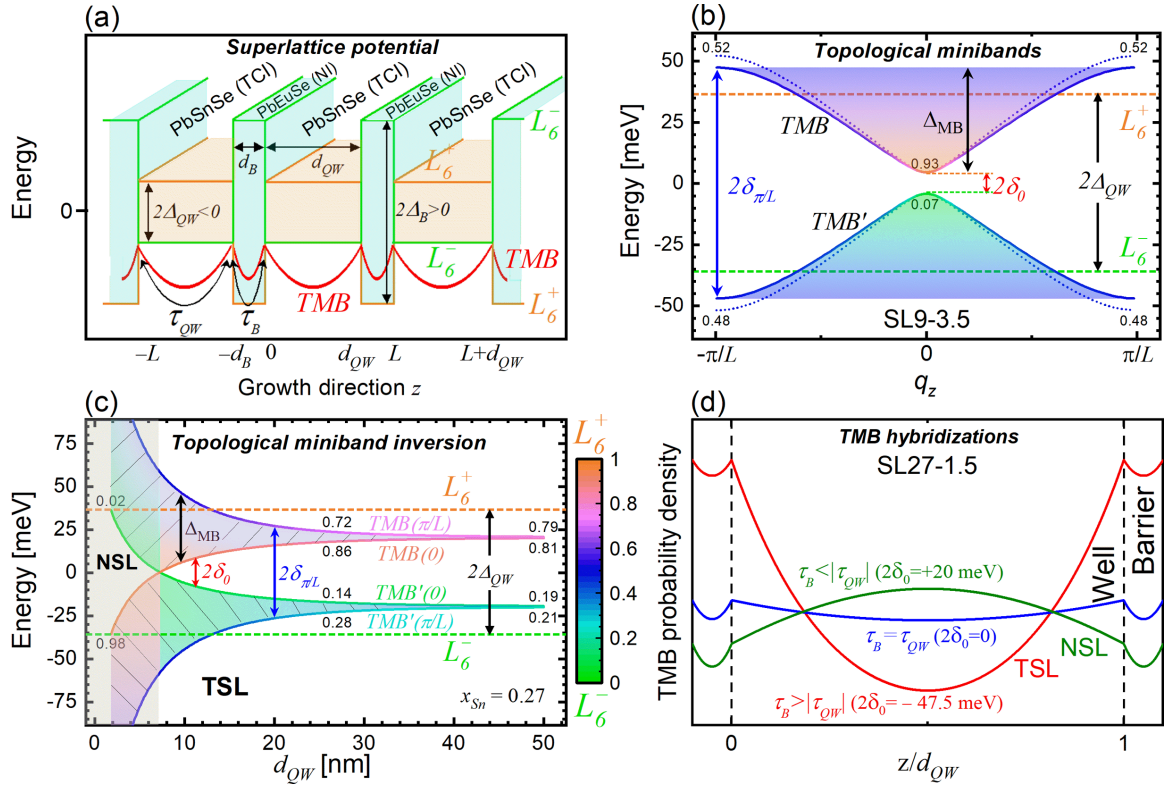| Parameter	SL9-3.5	SL27-1.5	SL15-3.5
TCI: d_{QW} (nm)	9 ± 0.2	27 ± 0.2	15 ± 0.2
x_{Sn} in $Pb_{1-x}Sn_xSe$	0.27 ± 0.01	0.26 ± 0.01	0.22 ± 0.01
Band gap $2\Delta_{QW}$ at 4 K (meV)	-72.5	-60	-20
NI: d_B (nm)	3.5 ± 0.2	1.5 ± 0.2	3.5 ± 0.2
y_{Eu} in $Pb_{1-y-x}Eu_ySn_xSe$	0.05	0.05	0.05
Band gap $2\Delta_B$ at 4 K (meV)	150	140	150
SL: Number N of periods	40	20	30
Miniband gap $2\delta_0$ at 4 K (meV)	-10	-47.5	$+10$
$|\tau_{QW}/\tau_B|$ at 4 K	0.80	0.14	1.75

FIG. 2. Topological miniband (TMB) formation in topological crystalline insulator (TCI)/normal insulator (NI) superlattices (SLs). (a) Modulation of the conduction and valence band edges along the SL structure in the growth direction z. The envelope wave function of the TMB concentrated at the interface is illustrated by the red curve; the black arrows indicate the intrawell and interwell tunnel coupling τ_{QW} and τ_B, respectively. (b) Miniband dispersion $E(q_z)$ for the longitudinal (solid lines) and oblique valleys (dashed lines) derived by $\boldsymbol{k} \cdot \boldsymbol{p}$ theory at $k_x = k_y = 0$ and 4.2 K for the SL structure SL9-3.5 listed in Table I. The color scale represents the symmetry (L_6^+ vs L_6^-) of the minibands [see scale bar in (c)]. Label numbers denote the L_6^+ proportion. (c) Evolution of the minibands and their symmetry (color scale) in the conduction and valence bands (TMB, respectively, TMB′) as a function of $Pb_{1-x}Sn_xSe$ thickness d_{QW}. The barrier width is fixed to $d_B = 3.5$ nm and the $Pb_{1-x}Sn_xSe$ composition to $x_{Sn} = 0.27$. The corresponding bulk band gaps are $2\Delta_{QW} = -72.5$ meV (dashed horizontal lines) and $2\Delta_B = +150$ meV. (d) Probability density of the TMB envelope wave function across the SL structure for different miniband topologies. Green line: normal SL (NSL) with $2\delta_0 = +20$ meV and $\tau_B < |\tau_{QW}|$, blue line: zero gap SL with $2\delta_0 = 0$ and $\tau_B = |\tau_{QW}|$, red line: topological SL (TSL) with $2\delta_0 = -47.5$ meV and $\tau_B > |\tau_{QW}|$. The different character is set by changing the $Pb_{1-x}Sn_xSe$ band gap from $2\Delta_{QW} = 10, -10, -60$ meV.

anisotropic band dispersion of the barriers to the otherwise isotropic $Pb_{1-x}Sn_xSe$ QWs [30,49], which yields slightly different v_z, the Dirac velocities along the $z//[111]$ growth direction for the longitudinal and oblique valleys. Note that we define here the Dirac velocity as the slope of the linear part of the $E(k)$ dispersion.

Solution of the $\boldsymbol{k} \cdot \boldsymbol{p}$ Hamiltonian yields the size of the miniband gaps $2\delta_0$ and $2\delta_{\pi/L}$ as a function of layer thicknesses and compositions. The results are exemplified in Fig. 2(c), where the evolution of the minibands is shown as a function of QW thickness for a fixed barrier thickness $d_B = 3.5$ nm and bulk band gaps set to $2\Delta_{QW} = -72.5$ meV and $2\Delta_B = +150$ meV, respectively. Evidently, the gap between the minibands goes to zero at a critical QW thickness (vertical line), indicating that only at sufficiently large d_{QW}, the symmetry of the band edges is inverted.

Based on the solution of the $\boldsymbol{k} \cdot \boldsymbol{p}$ model, we find that, in a good approximation, the $\delta(q_z)$ dispersion of the miniband

edges is given by (see Appendix B)

$$\delta(q_z) \cong \sqrt{\frac{2\hbar^2 v_z^2[1 - \cos(q_z L)]}{L^2} + \delta_0^2}, \quad (1a)$$

$$\delta_0 = \delta(q_z = 0) \cong \frac{d_{QW}\Delta_{QW} + d_B\Delta_B}{L}. \quad (1b)$$

This means that the hybridization gap $2\delta_0$ of the SL structure is essentially equal to the average of QW and barrier band gaps weighted according to their layer thickness. This is due to the close similarity of the band parameters of the layers. According to Eqs. (1a) and (1b), the minibands can be fully designed by the SL structure. Most importantly, the gap assumes a negative value only under the condition that $d_B\Delta_B < |d_{QW}\Delta_{QW}|$ and Δ_{QW} is negative. This means that a nontrivial miniband topology is not simply formed when the band gap of the TI well material is inverted.

We further identify the intrawell and interwell coupling strength τ_{QW} and τ_B between the TI/NI interfaces as $\tau_{QW} \equiv -\hbar v_z/d_{QW}\Delta_{QW}$ and $\tau_B \equiv \hbar v_z/d_B\Delta_B$, respectively. Note that, in Dirac matter, the penetration depth of the topological state is given by $\lambda_{QW} = \hbar v_z/|\Delta_{QW}|$ or $\lambda_B = \hbar v_z/\Delta_B$ in the well and in the barrier, respectively [19,50,51]. This means that $\tau_{QW} = \lambda_{QW}/d_{QW}$ and $\tau_B = \lambda_B/d_B$ capture the recovery of the topological state wave functions coming from two distinct interfaces separated by d_{QW} or d_B. We can then define the strong coupling limit when $|\tau_{QW,B}| > 1$, which insures significant interactions between interface states.

Using the expression of τ_{QW} and τ_B, Eq. (1b) simplifies to $\delta_0 = \hbar v_z(\tau_B^{-1} - \tau_{QW}^{-1})/L$. The topological phase transition where δ_0 is zero then occurs under the condition that

$$d_{QW}\Delta_{QW} + d_B\Delta_B = 0 \quad \text{or} \quad \tau_B = \tau_{QW}. \quad (2)$$

This leads to a change of the symmetry of the miniband states (L_6^+ vs L_6^-) that is represented by the color scale in Fig. 2(c), as further detailed in Appendix C. This shows that indeed, above a critical thickness, where $\tau_B > |\tau_{QW}|$, the character of the minibands is inverted, i.e., the SLs become topologically nontrivial [3,7]. The topological character is thus encoded in the $|\tau_{QW}/\tau_B|$ ratio that is <1 for the nontrivial, but >1 for trivial structures.

The pronounced effect of the band topology on the wave functions of the minibands is demonstrated by Fig. 2(d), where the wave function probability density across the QW and barriers is depicted for three cases, i.e., a normal SL (NSL) with $2\delta_0 > 0$, a zero gap SL, and a topological SL (TSL) with $2\delta_0 < 0$. Whereas, for the NSL with $\tau_B < |\tau_{QW}|$ [green line in Fig. 2(d)], the probability density is maximal in the center of the QW, as it is generic for conventional semiconductor SLs, this is exactly opposite for the TSL, with $\tau_B > |\tau_{QW}|$ (red line), where the probability density is minimal in the QW and high in the barriers. This remarkable difference is a clear signature of the topological character of the structure. At the phase transition between the NSL and TSL cases, the miniband gap is zero, and $\tau_B = |\tau_{QW}|$. As a result, the average probability density is the same in the QWs and barriers [blue line in Fig. 2(d)], i.e., the electrons/holes are evenly distributed over the QWs and barriers and thus most delocalized in the SL structure.

The coupling strengths τ_{QW} and τ_B directly control the miniband widths Δ_{MB} [shaded regions in Fig. 2(c)]. Accordingly, when layer thicknesses are reduced to a few nanometers, a strong coupling regime emerges, witnessed by a drastic widening of the minibands. Conversely, when the wells and/or barriers are thick, the coupling between the interfaces is diminished, narrowing the minibands, as seen in Fig. 2(c). In the thick barrier limit, uncoupled QWs are formed in which the interface states no longer hybridize across the barrier layers [19]. Accordingly, not only the band gaps but also miniband widths can be engineered by control of the layer thicknesses.

For our magneto-optical experiments, two types of samples were prepared, namely, TSLs designated to exhibit a negative miniband gap and nontrivial topology (samples SL9-3.5 and SL27-1.5, see Table I), and NSLs with reduced Sn content. The Sn content is a crucial parameter that controls the well potential depth. It is reduced for SL15-3.5, rendering the SL

gap positive. SL15-3.5 is therefore a control sample with trivial topology. In the samples, the QW and barrier thicknesses were varied to yield different coupling strengths and miniband widths. The miniband gaps $2\delta_0$ and coupling ratios $|\tau_{QW}/\tau_B|$ at 4 K are also listed in Table I, where $|\tau_{QW}/\tau_B|$ < 1 for topological SL9-3.5 and SL27-1.5, but >1 for the trivial SL15-3.5 reference sample. It is noted that, due to the small lattice mismatch between the QW and barrier materials, a small tensile strain is imposed in the QWs, and the barriers are slightly compressed. This leads to small deviations in the band gaps Δ_{QW} and Δ_B with respect to the unstrained bulk material [30,33].

IV. LANDAU LEVEL SPECTROSCOPY OF TMBS

To assess the TMBs, magneto-optical spectroscopy was performed in Faraday geometry at magnetic fields up to 15 T [19,52]. The results for SL9-3.5 and SL15-3.5 are shown in Fig. 3 for $T = 4.2$ and 160 K. In both cases, many Landau level transitions are observed [arrows in Figs. 3(a) and 3(b)], shifting to higher energies as the magnetic field increases. From this, we construct fan charts shown in Figs. 3(c) and 3(d), where each data point corresponds to a minimum in the transmission spectra in (a) and (b). The fan charts are analyzed using Landau level transitions obtained from $\boldsymbol{k} \cdot \boldsymbol{p}$ calculations presented in Appendix D (solid and dashed lines) and fitted to the experimental data. From the analysis, we unambiguously identify the existence of two individual subsets of transitions, indicated in Fig. 3 by the red and blue colors. These are identified to occur at the miniband extrema at $q_z = 0$ (red) and $q_z = \pm\pi/L$ (blue), respectively, where the joint density of states of the minibands is maximal. Each extrapolates to a different energy at $B = 0$, corresponding to the miniband gaps $2\delta_0$ and $2\delta_{\pi/L}$ at the center and edge of the SL BZ, respectively, in perfect agreement with the $\boldsymbol{k} \cdot \boldsymbol{p}$ calculations. The validity of the assignment is evidenced by the perfect fit obtained in each case, with the fit parameters listed in the Supplemental Material [53]. Most importantly, the observation of the two independent series of transitions directly proves the miniband formation in our strongly coupled SL structures.

For the SL9-3.5, the extrapolation of the data points yields a miniband gap of $|2\delta_0| = 10 \pm 5$ meV at 4.2 K, whereas the second set of transitions yields a gap of $|2\delta_{\pi/L}| = 95 \pm 5$ meV at the boundary of the BZ. Both values perfectly agree with the calculated values in Fig. 2(c) for the given TI/NI layer thicknesses. Using $\Delta_{MB} = |\delta_0 - \delta_{\pi/L}|$, a miniband width of 42.5 ± 10 meV is derived for this sample. According to the $\boldsymbol{k} \cdot \boldsymbol{p}$ calculations [cf., Fig. 2(c)], the miniband gap is inverted, i.e., the minibands are topologically nontrivial at 4.2 K. This is supported by the fact that the in-plane Dirac velocities, determined from the fits for the longitudinal and oblique valleys ($v_\parallel^l = 4.40 \times 10^5$ m/s and $v_\parallel^o = 4.10 \times 10^5$ m/s) are below the critical values where the band gap is inverted [31]. It is noted that the small difference in the in-plane miniband dispersion for the longitudinal and oblique valleys arises from the admixture of the band anisotropy of the $Pb_{1-y-x}Eu_ySn_xSe$ barriers to that of the QWs caused by the large extent of the wave function across the SL period, as the bulk bands of $Pb_{1-x}Sn_xSe$ with $0.21 < x_{Sn} < 0.29$ are otherwise isotropic. This is particularly pronounced for topological
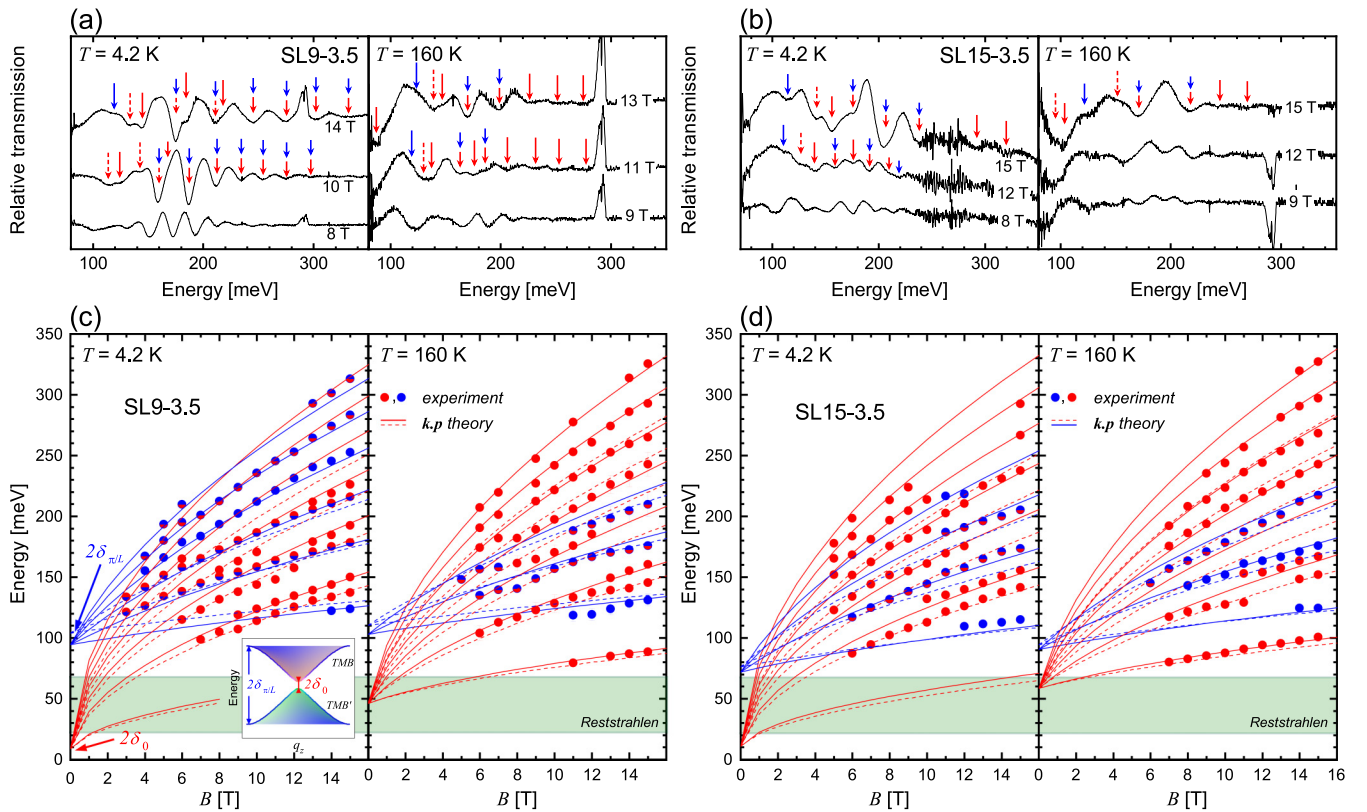
FIG. 3. Magneto-optical spectroscopy. (a) and (b) Normalized transmission spectra of the superlattice (SL) samples SL9-3.5 and SL15-3.5 at 4.2 and 160 K at different magnetic fields of up to $B = 15$ T. The minima are due to Landau level transitions between the minibands at $q_z = 0$ and $q_z = \pi/L$, marked by red and blue arrows, respectively. (c) and (d) Magneto-optical fan charts derived from the experiments (red/blue dots) compared with the calculations by the $\boldsymbol{k} \cdot \boldsymbol{p}$ model for the longitudinal and oblique valleys (solid and dashed lines, respectively). The extrapolated transition energies $2\delta_0$ and $2\delta_{\pi/L}$ at $B = 0$ of the two transition sets are indicated by the arrows and in the insert. The green shaded regions indicate the experimentally nonaccessible energy range blocked by the reststrahlen band of the substrate and window cutoffs.

SLs because the probability density of the wave function is strongly enhanced within the barriers, as shown by Fig. 2(d). For the second SL sample SL15-3.5 with lower Sn content, the same analysis yields $2\delta_0 = +10 \pm 5$ meV and $2\delta_{\pi/L} = 74 \pm 5$ meV, rendering the gap positive and the minibands topologically trivial. Moreover, due to the increased QW thickness of $d_{\mathrm{QW}} = 15$ nm, the miniband width is reduced to $\Delta_{\mathrm{MB}} = 32 \pm 10$ meV, following nicely the trend of Fig. 2(c).

We highlight that the observed magneto-optical transitions occur both at $q_z = 0$ and $q_z = \pi/L$, where the joint density of states for optical transitions is largest. The fact that both transitions are simultaneously observed and precisely fit to the calculations evidences the existence of minibands in the SL structures. To this end, we emphasize that the higher energy transitions (marked in blue) cannot be interpreted as transitions between higher energy excited states or higher order minibands. Indeed, for the samples in Fig. 3, these would lie in the continuum above the band gap $2\Delta_B$ of the barrier material, as shown in the Supplemental Material [53]. Consequently, we safely attribute the observed absorptions to the emergent minibands caused by the hybridization of interface states.

V. EXPERIMENTAL DEMONSTRATION OF SYMMETRY INVERSION

The topological character of the SL structures is directly revealed by magneto-optical measurements at varying tem-

peratures in which the fundamental band gaps of the QW and barrier materials are tuned [26,30,31]. First, we focus on the SL27-1.5 that displays the largest negative miniband gap at 4.2 K and is thus most deeply in the inverted topological region. The magneto-optical fan chart of the sample shown in Fig. 4(a) yields a miniband gap of $2\delta_0 = -47.5 \pm 2.5$ meV and $2\delta_{\pi/L} = -75 \pm 5$ meV at 4.2 K, as indicated by the solid lines extrapolated to $B = 0$. Figure 4(b) displays the corresponding transmission spectra at a fixed magnetic field of 15 T as a function of temperature from 4.2 to 225 K. Clearly, the first interband transition occurring at $q_z = 0$, highlighted by the red dots, exhibits a nonmonotonic behavior in its position, shifting initially to lower energies as the temperature increases, but then reverses and shifts in the opposite direction >160 K.

The shifts are summarized in Fig. 4(c), where the experimental data (red dots) are compared with the $\boldsymbol{k} \cdot \boldsymbol{p}$ calculations (red line). Evidently, the nonmonotonic shift is perfectly reproduced by our model. The effect originates from the anomalous temperature dependence of the band gaps of IV–VI materials in which the TCI band inversion is induced by the sp repulsion between the L bands and lower lying S bands rather than by spin-orbit coupling [54]. This repulsion decreases with increasing interatomic distances, which lifts the band inversion and renders the material trivial as the temperature is increased. The same also occurs in our TCI/NI structures,
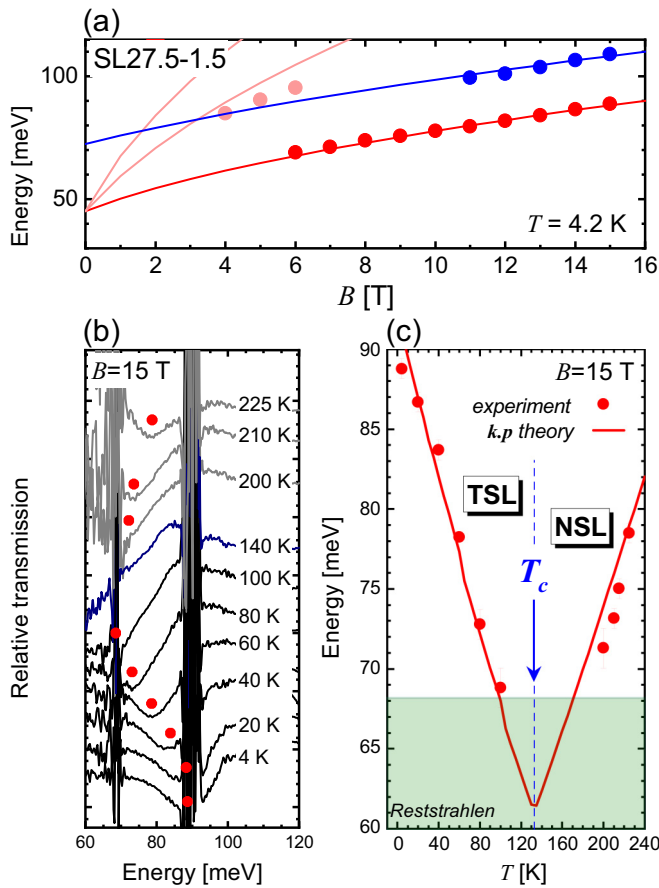
FIG. 4. Temperature dependence of the miniband gap. (a) Magneto-optical fan chart of superlattice (SL) SL27-1.5 at 4.2 K, showing the ground transitions between the minibands at $q_z = 0$ (red) and $|q_z| = \pi/L$ (blue) on an enlarged scale. (b) Temperature dependence of the far-infrared transmission spectra at $B = 15$ T in which the lowest energy transition is indicated by the red dots. The energy position of this transition is shown in (c) as a function of temperature together with the theoretical fit (solid line) obtained by the $k \cdot p$ model. The critical temperature $T_c \cong 130$ K, indicated by the blue arrow, separates the topological SL (TSL) from the normal SL (NSL) phases and where $\partial|\delta_0|/\partial T$ changes sign. Note that transitions <70 meV are masked by the reststrahlen band of the substrate.

albeit at a different critical temperature T_c because the SL miniband inversion is not only governed by the bulk bands, but also by the thicknesses of the well and barrier materials [Eqs. (1a) and (1b)]. Most importantly, the abrupt sign change of $\partial|\delta|/\partial T$ of the TSL structure is clear evidence for the occurrence of this topological phase transition, with a critical temperature $T_c \approx 130$ K in this sample, below which $\partial|\delta|/\partial T$ is negative. This is the hallmark for the topological nature of our TCI/NI SL system.

The nonmonotonic behavior is to be contrasted with our previous observations for TCI multi-QW structures [19], where due to an order of magnitude wider barriers ($d_B > 35$ nm), the coupling between the TISs across the barriers is negligible ($\tau_B \approx 0$). As a result, no minibands are formed, and the hybridization gap of TIS states only monotonically increases with temperature, and thus, no sign changes occur.

In contrast, for the presently studied strong coupled structures, our experiments reveal that extended minibands are formed due to the strong interwell hybridization $\tau_B > 0$, inducing an emergent topological phase transition.

The complete dataset for all SL samples is summarized in Figs. 5(a)–5(c), which show the evolution of the miniband gaps $2\delta_0$ and $2\delta_{\pi/L}$ (red and blue dots, respectively) as a function of temperature together with the $k \cdot p$ calculations (solid lines). For all cases, theory and experiments perfectly fit to one another. The bulk band gaps $\Delta_{QW}(x, T)$ and $\Delta_B(y, T)$ obtained from the magneto-optical fits are shown as well for comparison by the open circles in Figs. 5(a)–5(c), and they agree very well with the empirical expressions (dashed lines) derived in our previous works [30,33]. For the two SLs SL9-3.5 and SL27-1.5, the minibands are inverted at cryogenic temperatures, and thus, they are topological nontrivial. Their absolute miniband gap value of $|2\delta_0|$ decreases with temperature and turns to positive values when the critical temperature T_c, indicated by the vertical dashed lines, is reached. This marks the topological phase transition from a TSL to an NSL structure.

The derived T_c values are 40 and 130 K, respectively, which nicely agrees with the $k \cdot p$ calculations (solid lines). The difference in T_c is mainly due to the different barrier thicknesses (see Table I), for which reason the ratio $|\tau_{QW}/\tau_B|$ of SL9-3.5 is closer to 1 at 4.2 K than the one of SL27-1.5. The resulting weaker interwell coupling in SL9-3.5 makes it closer to the topological phase transition. For the third sample SL15-3.5 [Fig. 5(c)], the topological phase transition does not occur because it remains in the NSL phase down to 4.2 K, where $2\delta_0 = +10$ meV is still positive. Thus, it serves as a control sample that unequivocally reveals that the topological nature of the TSL is intrinsically coupled with the temperature-dependent topological phase transition. Moreover, it shows that the SL structures can be topologically trivial even if the QWs are in the TCI state.

Finally, we want to highlight that the topological character of the SL system is also encoded in the miniband widths Δ_{MB} represented by the shaded regions in Figs. 5(a)–5(c). For the TSLs in (a) and (b), the miniband width increases with increasing temperature, displaying a maximum at the TSL/NSL transition [arrows Figs. 5(a) and 5(b)] and thereafter again decreasing, whereas for the NSL [SL15-3.5, Fig. 5(c)], the miniband width only monotonically decreases. Accordingly, for the TSL, $\Delta_{MB}(T)$ displays a cusp at the topological phase transition, as shown in Fig. 5(f), both in theory (solid lines) and experiments (dots). This observation is therefore another clear-cut criterion for a topological phase transition in SLs. The cusp arises from the fact that the intrawell and interwell coupling strengths are equal when the gap $2\delta_0 = 0$, and thus, the miniband wave functions are maximally delocalized, maximizing the miniband width. To this end, we refer to Fig. 2(d), which illustrates the calculated probability density of SL27-1.5 TMB at 4.2 K (in red), $T_C = 130$ K (in blue), and 200 K (olive). In fact, at the topological phase transition, where $2\delta_0 = 0$, the miniband width scales as $\Delta_{MB} \cong 2\hbar v_z/L$ following Eq. (1a). Remarkably, it is essentially independent of the QW and barrier thicknesses.

The topological phase transitions are put into broader perspective by the topological phase diagrams of Figs. 5(d) and
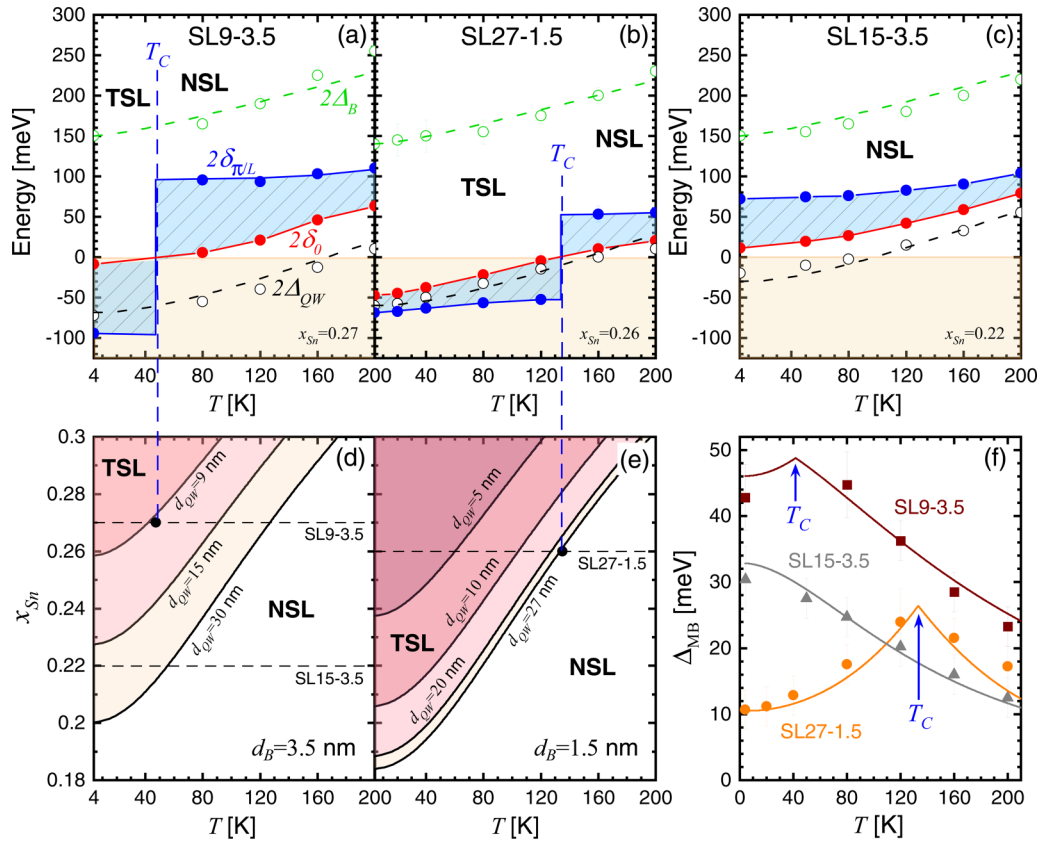
FIG. 5. Demonstration of topological phase transitions. (a)–(c) Temperature dependence of the superlattice (SL) miniband gaps $2\delta_0$ (red) and $2\delta_{\pi/L}$ (blue) at $q_z = 0$ and $\pm\pi/L$ obtained by experiments (dots) and $\boldsymbol{k} \cdot \boldsymbol{p}$ model (solid lines). The region of the miniband band inversion is highlighted in yellow. The vertical dashed lines indicate the critical temperature T_c below which the SLs are nontrivial. Above T_c, they are trivial. This transition is due to a symmetry inversion which changes the sign of the miniband gaps. The blue shaded area represents twice the miniband width $2\Delta_{MB}$. Also shown is the temperature dependence of the band gaps of the quantum well [QW; $2\Delta_{QW}(x, T)$, black circles] and the barriers [$2\Delta_B(y, T)$, green circles] obtained from the fits that nicely agree with our previous work (dashed lines) [30,33]. (d) and (e) Topological phase diagrams of the SL structures as a function of temperature and $Pb_{1-x}Sn_xSe$ composition for fixed barrier thickness of (d) $d_B = 3.5$ nm and (e) 1.5 nm. The solid lines represent the phase boundaries for different QW thicknesses d_{QW}, and the shaded regions indicate topological SL (TSL) phases. The black dots in the phase diagrams mark the experimental phase transitions observed for our samples. (f) Temperature dependence of the miniband width Δ_{MB} derived from experiments (symbols) and the $\boldsymbol{k} \cdot \boldsymbol{p}$ model (solid lines). The cusps mark the topological-to-normal insulator SL phase transition, as indicated by the arrows.

5(e). These display the topological state and the phase boundaries between the TSL and NSL structures as a function of QW composition and temperature for different QW thicknesses (solid lines) but fixed barrier thickness $d_B = 3.5$ and 1.5 nm. As indicated by the experimental data points (black dots) obtained from Figs. 5(a) and 5(b), these phase diagrams are in excellent agreement with our experiments. Therefore, they accurately describe the topological character of the system and serve as guides for engineering the miniband properties for a given application.

VI. CONCLUSION

Using Landau level spectroscopy, we have demonstrated the formation of TMBs in artificial TCI/NI SLs obtained by molecular beam epitaxy and band structure engineering of IV–VI semiconductor heterostructures. By envelope function calculations, we revealed that the minibands are the offspring of

the hybridized TISs that tunnel couple both across the NI barrier layers as well as across the TI QWs. In the topological SL state, this gives rise to a pronounced shift of the wave function envelope from the QWs to the barriers, which discriminates the TSL from NSL structures. As a result, the topological phase as well as miniband gap dispersions can be perfectly controlled by the layer thicknesses and compositions, and tunable miniband gaps and miniband widths are attained. The temperature-induced phase transition of the miniband topological character is in perfect agreement with our theoretical model. Thereby, we experimentally demonstrate the recently predicted Burkov-Balents phase diagram [3]. Accordingly, our TI/NI SLs provide a quasi-3D topological state that can be engineered over a wide range, which offers avenues toward nonzero dissipation less spin Hall currents [3]. Moreover, by breaking time reversal symmetry using magnetic doping [37,55–57], magnetic topological SLs with tunable Weyl or even line node semimetal phases [3,7,8] can be reached.

APPENDIX A: $k \cdot p$ MODEL FOR SLS

The stacking of $Pb_{1-x}Sn_xSe$ and $Pb_{1-y-x}Sn_xEu_ySe$ layers makes z-dependent L_6^- and L_6^+ band edges, where z is the growth axis. At the interfaces between two layers, the bands of the same symmetry must be connected [42], thus leading to a potential that inverses the conduction and valence bands at each interface. As the system is considered electron-hole symmetric [33], this potential can be modeled by a z-dependent energy gap $\Delta(z)$ that changes sign across each interface. Due to confinement, k_z is not a good quantum number and is replaced by its operator value $-i\partial/\partial z$. The k^2 terms coming from the interactions between L_6^- or L_6^+ with other bands located at much higher or lower energies are neglected [58]. We also consider a magnetic field along the z axis. In this way, for $n > 0$ (n being the Landau level index), the Hamiltonian of the SL system can be written in the basis $L_6^+\alpha|n-1\rangle; L_6^+\beta|n\rangle; L_6^-\alpha|n-1\rangle; L_6^-\beta|n\rangle$ ($|n\rangle$ being the harmonic oscillator functions) as [19,46,59]

$$
\begin{pmatrix}
-\Delta(z) & 0 & -i\hbar v_z \frac{\partial}{\partial z} & v_\parallel \sqrt{2e\hbar Bn} \\
0 & -\Delta(z) & v_\parallel \sqrt{2e\hbar Bn} & i\hbar v_z \frac{\partial}{\partial z} \\
-i\hbar v_z \frac{\partial}{\partial z} & v_\parallel \sqrt{2e\hbar Bn} & \Delta(z) & 0 \\
v_\parallel \sqrt{2e\hbar Bn} & i\hbar v_z \frac{\partial}{\partial z} & 0 & \Delta(z)
\end{pmatrix},
\tag{A1}
$$

where α and β are the spins with underlying spin-orbit coupling; v_z and $v_\parallel$ are the electron velocities, respectively, along

and perpendicular to the growth direction. The jth energy and wave functions of the confined states at $k_x = k_y = 0$ are calculated by reducing the Hamiltonian in Eq. (A1) accordingly. This yields two spin-decoupled equations:

$$
\begin{pmatrix}
-\Delta(z) - E_j & \xi i\hbar v_z \frac{\partial}{\partial z} \\
\xi i\hbar v_z \frac{\partial}{\partial z} & \Delta(z) - E_j
\end{pmatrix}
\begin{pmatrix}
F_1^{(j)} \\
\xi F_2^{(j)}
\end{pmatrix} = 0,
$$

where $\xi = \pm$ represents the spins, and E_j denotes the spin-degenerated energy of the jth confined states and goes along with their two-component spinor envelope wave functions. The envelope wave function of the jth confined states have a L_6^+ and a L_6^- component: $F_1^{(j)}$ and $F_2^{(j)}$, respectively.

To calculate each component of each envelope function, the current probability continuity conditions are applied at each interface for the L_6^+ component $F_1^{(j)}$. Therefore, at the interface between the well and the barrier, $F_1^{(j)}$ must be continuous as well as the quantity [43,44]

$$
\frac{1}{\Delta(z) - E_j} \frac{\partial F_1^{(j)}}{\partial z}.
\tag{A2}
$$

Here, $F_2^{(j)}$ is then deduced from $F_1^{(j)}$ by

$$
F_2^{(j)}(z) = \frac{i\hbar v_z}{\Delta(z) - E_j} \frac{\partial F_1^{(j)}}{\partial z}.
$$

The SL periodicity implies that $F_1^{(j)}$ can be written as a Bloch wave: $F_1^{(j)}(z+L) = F_1^{(j)}(z)e^{iq_z L}$ with $-\pi/L < q_z < +\pi/L$. If $|E_j| < |\Delta_{QW}|$, the continuity of $F_1^{(j)}$ and Eq. (A2) at $z = d_{QW}$ and $z = L$ yields a four-equation system giving the following secular equation:

$$
\cos(q_z L) = \cosh(\kappa d_{QW})\cosh(\rho d_B) - \frac{1}{2}\left(\gamma + \frac{1}{\gamma}\right)\sinh(\kappa d_{QW})\sinh(\rho d_B),
\tag{A3}
$$

with $\gamma = -\frac{\kappa}{\rho}\frac{E_j - \Delta_B}{E_j - \Delta_{QW}}$; $\kappa = \frac{1}{\hbar v_z}\sqrt{\Delta_{QW}^2 - E_j^2}$; and $\rho = \frac{1}{\hbar v_z}\sqrt{\Delta_B^2 - E_j^2}$.

Here, we have written $F_1^{(j)}$ as

$$
F_1^{(j)}(z) = \begin{cases}
a\cosh(\kappa z) + b\cosh(\kappa z), & \text{in the well} \\
c\cosh[\rho(z - d_{QW})] + d\cosh[\rho(z - d_{QW})], & \text{in the barrier},
\end{cases}
$$

where a, b, c, and d are the four eigenvector components of the system. For a negative enough Δ_{QW}, Eq. (A3) gives two solutions that describe TMB and TMB′ dispersions vs q_z at $k_x = k_y = 0$, as it is shown in Figs. 2(b) and 2(c). Here, $F_1^{(j)}$ is then deduced and shown, for instance, in Fig. 2(d). For a miniband with $|E_j| > |\Delta_{QW}|$, Eq. (A3) is transformed into

$$
\cos(q_z L) = \cos(kd_{QW})\cosh(\rho d_B) - \frac{1}{2}\left(\tilde{\gamma} - \frac{1}{\tilde{\gamma}}\right)
$$
$$
\times \sin(kd_{QW})\sinh(\rho d_B),
$$

with $\tilde{\gamma} = \frac{k}{\rho}\frac{E_j - \Delta_B}{E_j - \Delta_{QW}}$ and $k = \frac{1}{\hbar v_z}\sqrt{E_j^2 - \Delta_{QW}^2}$.

APPENDIX B: APPROXIMATION OF THE MINIBAND DISPERSION

Equation (A3) can be approximated if the cosh and sinh functions are developed to the second order. One gets with $E_j = \delta$

$$
\cos(q_z L) \cong 1 + \frac{\kappa^2 d_{QW}^2}{2} + \frac{\rho^2 d_B^2}{2} - \frac{1}{2}\left(\gamma + \frac{1}{\gamma}\right)\kappa d_{QW}\rho d_B,
$$

$$
\Leftrightarrow \delta(q_z) \cong \sqrt{\frac{2\hbar^2 v_z^2[1 - \cos(q_z L)] + (d_{QW}\Delta_{QW} + d_B\Delta_B)^2}{L^2}},
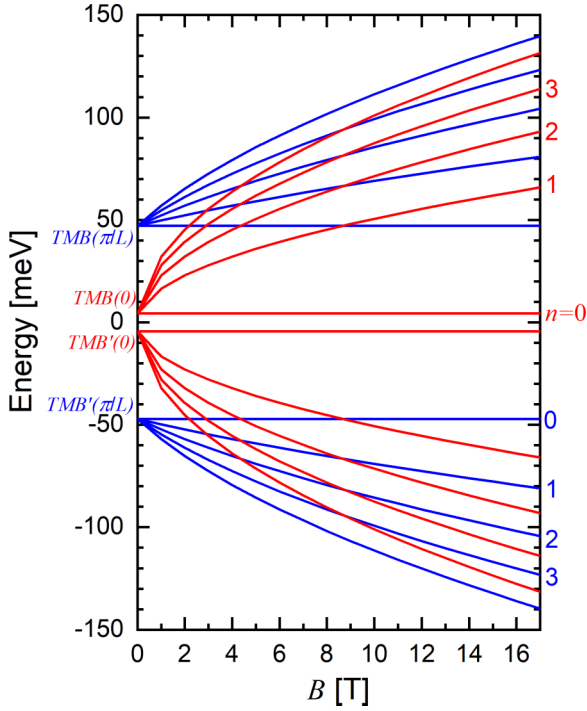$$

FIG. 6. Landau levels of the topological minibands (TMBs). Calculated Landau levels of TMB and TMB′ at $q_z = 0$ (red) and $q_z = \pm\pi/L$ (blue). Calculations have been performed with the parameters $d_{QW} = 9$ nm, $d_B = 3.5$ nm, $2\Delta_{QW} = -72.5$ meV, $2\Delta_B = +150$ meV, and $v_\parallel = v_z = 4.40 \times 10^5$ m/s. Some Landau level indexes n are written at the right.

which is Eqs. (1a) and (1b). The approximation $\rho d_B \sim 0$ is justified, as the investigated SLs have ultrathin barriers. Small values of κd_{QW} are obtained if the wells are thin or if δ is close to Δ_{QW}, which is the case in this paper.

APPENDIX C: SYMMETRY INVERSION OF THE MINIBANDS

A symmetry inversion can be induced by the interwell coupling τ_B in a SL. Indeed, one can notice that the SL gap

$2\delta_0$ is vanishing at a certain point [see Fig. 2(c), for instance]. Having a bound state at the middle of the QW energy gap implies that $E_j = 0$, and therefore, $\kappa = \frac{|\Delta_{QW}|}{\hbar v_z}$, $\rho = \frac{\Delta_B}{\hbar v_z}$, and $\gamma = 1$. Equation (A3) thus becomes

$$\cos(q_z L) = \cosh(\kappa d_{QW}) \cosh(\rho d_B) - \sinh(\kappa d_{QW}) \sinh(\rho d_B)$$
$$= \cosh(\kappa d_{QW} - \rho d_B).$$

We conclude that, for $d_B \Delta_B = d_{QW}|\Delta_{QW}|$, or $\tau_B = \tau_{QW}$, we have $\delta_0 = 0$, and Eq. (2) is retrieved. The calculations give an inversion of the minibands. To discriminate the topological phase from the trivial one, the exact symmetry of the bound states at $q_z = 0$ and $|q_z| = \pi/L$ have been numerically calculated. The L_6^+ symmetry of the jth confined states is calculated as $\int F_1^{(j)} F_1^{(j)} dz$, where the integral extends over one SL period: $0 \leqslant z \leqslant L$. One can then deduce the L_6^- parity by $1 - \int F_1^{(j)} F_1^{(j)} dz$. A symmetry inversion is found when the state with a L_6^+ major component lies above the L_6^- major state, and one can retrieve the Burkov-Balents phase diagram [3].

The results of the symmetry calculations are given in Figs. 2(b) and 2(c) of the main text. We deduce that, at 4.2 K, both SL9-3.5 and SL27-1.5 display symmetry inverted miniband structure. This inversion is then experimentally demonstrated for SL27-1.5 (see Fig. 4). Oppositely, SL15-3.5 presents a normal symmetry order mainly because, for its given layer thicknesses, $2\Delta_{QW} = -20$ meV is not enough.

APPENDIX D: LANDAU LEVELS OF THE MINIBANDS

The B-dependent terms in Eq. (A1) are considered in a perturbation theory. The perturbative Hamiltonian for $n > 0$ is then

$$\begin{pmatrix} 0 & 0 & 0 & v_\parallel\sqrt{2e\hbar Bn} \\ 0 & 0 & v_\parallel\sqrt{2e\hbar Bn} & 0 \\ 0 & v_\parallel\sqrt{2e\hbar Bn} & 0 & 0 \\ v_\parallel\sqrt{2e\hbar Bn} & 0 & 0 & 0 \end{pmatrix}.$$

We derive an effective Hamiltonian expressed in the basis of the normalized envelope functions of TMB and TMB′ obtained above at $k_x = k_y = 0$ and for a given q_z. It gives

$$H_{TMB-TMB'}^{eff}(q_z) = \begin{bmatrix} -\delta(q_z) & 0 & 0 & Av_\parallel\sqrt{2e\hbar Bn} \\ 0 & -\delta(q_z) & Av_\parallel\sqrt{2e\hbar Bn} & 0 \\ 0 & Av_\parallel\sqrt{2e\hbar Bn} & \delta(q_z) & 0 \\ Av_\parallel\sqrt{2e\hbar Bn} & 0 & 0 & \delta(q_z) \end{bmatrix},$$

where $A = \int [F_1^{(TMB)} F_2^{(TMB')} + F_1^{(TMB')} F_2^{(TMB)}] dz = \pm i$ by parity. Therefore, the twofold degenerated Landau levels for $n > 0$ are those of Dirac fermions:

$$E_n = \pm\sqrt{\delta^2(q_z) + 2e\hbar v_\parallel^2 Bn}. \tag{D1}$$

In this system, the $n = 0$ Landau levels are spin polarized and nondispersive in magnetic field. The corresponding Landau levels are given in Fig. 6. In this paper, experiments have been performed in the Faraday geometry that leads to conventional dipole selection rules. Magneto-optical transitions are thus occurring between two Landau levels $n \to n \pm 1$ and at

fixed q_z. For instance, the ground transition observed in Fig. 4 involves the levels 0 of TMB′ and 1 from TMB.

More subtly, we want to point out that the perturbative Hamiltonian is exact for the longitudinal valley, whose high-symmetry axis is naturally aligned with $B//[111]$; however, it is not the case for the oblique valleys, whose main axis is

tilted from z by an angle $\theta = 70.5°$. This anisotropy effect has been considered by rotating spin and momentum operators in the Hamiltonian, an operation which is detailed in Ref. [60]. This result allows us to adopt an empirical approach in this paper by modeling the anisotropy effect with different valley-dependent fitting parameters $v_{\parallel}$ and v_z in Eq. (D1).

[1] M. Serlin, C. L. Tschirhart, H. Polshyn, Y. Zhang, J. Zhu, K. Watanabe, T. Taniguchi, L. Balents, and A. F. Young, Intrinsic quantized anomalous Hall effect in a moiré heterostructure, Science **367**, 900 (2019).

[2] Y. Cao, V. Fatemi, S. Fang, K. Watanabe, T. Taniguchi, E. Kaxiras, and P. Jarillo-Herrero, Unconventional superconductivity in magic-angle graphene superlattices, Nature **556**, 43 (2018).

[3] A. A. Burkov and L. Balents, Weyl Semimetal in a Topological Insulator Multilayer, Phys. Rev. Lett. **107**, 127205 (2011).

[4] J. Wang, B. Lian, and S.-C. Zhang, Dynamical axion field in a magnetic topological insulator superlattice, Phys. Rev. B **93**, 045115 (2016).

[5] E. Tang and L. Fu, Strain-induced partially flat band, helical snake states and interface superconductivity in topological crystalline insulators, Nat. Phys. **10**, 964 (2014).

[6] F. Carosella, A. Wacker, R. Ferreira, and G. Bastard, One-dimensional massless Dirac bands in semiconductor superlattices, Phys. Rev. B **89**, 235301 (2014).

[7] A. A. Burkov, M. D. Hook, and L. Balents, Topological nodal semimetals, Phys. Rev. B **84**, 235126 (2011).

[8] C. Lei, S. Chen, and A. H. MacDonald, Magnetized topological insulator multilayers, Proc. Natl. Acad. Sci. USA **117**, 27224 (2020).

[9] T. Meng and L. Balents, Weyl superconductors, Phys. Rev. B **86**, 054504 (2012).

[10] C.-Z. Chang *et al.*, Experimental observation of the quantum anomalous Hall effect in a magnetic topological insulator, Science **340**, 167 (2013).

[11] R. Yu, W. Zhang, H.-J. Zhang, S.-C. Zhang, X. Dai, and Z. Fang, Quantized anomalous Hall effect in magnetic topological insulators, Science **329**, 61 (2010).

[12] C.-X. Liu, X.-L. Qi, X. Dai, Z. Fang, and S.-C. Zhang, Quantum Anomalous Hall Effect in Hg$_{1-y}$Mn$_y$Te Quantum Wells, Phys. Rev. Lett. **101**, 146802 (2008).

[13] Y. Tokura, K. Yasuda, and A. Tsukazaki, Magnetic topological insulators, Nat. Rev. Phys. **1**, 126 (2019).

[14] S. Ok, M. Legner, T. Neupert, and A. M. Cook, Magnetic Weyl and Dirac Kondo semimetal phases in heterostructures, arXiv:1703.03804.

[15] L. He, X. Kou, and K. L. Wang, Review of 3D topological insulator thin-film growth by molecular beam epitaxy and potential applications, Phys. Status Solidi RRL **7**, 50 (2013).

[16] T. P. Ginley, Y. Wang, and S. Law, Topological insulator film growth by molecular beam epitaxy: A review, Crystals **6**, 154 (2016).

[17] E. D. L. Rienks *et al.*, Large magnetic gap at the Dirac point in Bi$_2$Te$_3$/MnBi$_2$Te$_4$ heterostructures, Nature **576**, 423 (2019).

[18] P. P. Shibayev, E. J. König, M. Salehi, J. Moon, M.-G. Han, and S. Oh, Engineering topological superlattices and phase diagrams, Nano Lett. **19**, 716 (2019).

[19] G. Krizman, B. A. Assaf, T. Phuphachong, G. Bauer, G. Springholz, G. Bastard, R. Ferreira, L. A. de Vaulchier, and Y. Guldner, Tunable Dirac interface states in topological superlattices, Phys. Rev. B **98**, 075303 (2018).

[20] I. Levy, C. Youmans, T. A. Garcia, H. Deng, S. Alsheimer, C. Testelin, L. Krusin-Elbaum, P. Ghaemi, and M. C. Tamargo, Designer topological insulator with enhanced gap and suppressed bulk conduction in Bi$_2$Se$_3$/Sb$_2$Te$_3$ ultrashort-period superlattices, Nano Lett. **20**, 3420 (2020).

[21] I. Belopolski *et al.*, A novel artificial condensed matter lattice and a new platform for one-dimensional topological phases, Sci. Adv. **3**, e1501692 (2017).

[22] J. Tominaga, N. Miyata, S. Sumi, H. Awano, and S. Murakami, Topologically protected spin diffusion and spin generator using chalcogenide superlattices, Npj 2D Mater. Appl. **4**, 22 (2020).

[23] Y. Zhao, H. Liu, X. Guo, Y. Jiang, Y. Sun, H. Wang, Y. Wang, H.-D. Li, M.-H. Xie, X.-C. Xie, and J. Wang, Crossover from 3D to 2D quantum transport in Bi$_2$Se$_3$/In$_2$Se$_3$ superlattices, Nano Lett. **14**, 5244 (2014).

[24] T. H. Hsieh, H. Lin, J. Liu, W. Duan, A. Bansil, and L. Fu, Topological crystalline insulators in the SnTe material class, Nat. Commun. **3**, 982 (2012).

[25] L. Fu, Topological Crystalline Insulators, Phys. Rev. Lett. **106**, 106802 (2011).

[26] P. Dziawa, B. J. Kowalski, K. Dybko, R. Buczko, A. Szczerbakow, M. Szot, E. Łusakowska, T. Balasubramanian, B. M. Wojek, M. H. Berntsen, O. Tjernberg, and T. Story, Topological crystalline insulator states in Pb$_{1-x}$Sn$_x$Se, Nat. Mater. **11**, 1023 (2012).

[27] S.-Y. Xu *et al.*, Observation of a topological crystalline insulator phase and topological phase transition in Pb$_{1-x}$Sn$_x$Te, Nat. Commun. **3**, 1192 (2012).

[28] C. Yan, J. Liu, Y. Zang, J. Wang, Z. Wang, P. Wang, Z.-D. Zhang, L. Wang, X. Ma, S. Ji, K. He, L. Fu, W. Duan, Q.-K. Xue, and X. Chen, Experimental Observation of Dirac-like Surface States and Topological Phase Transition in Pb$_{1-x}$Sn$_x$Te(111) Films, Phys. Rev. Lett. **112**, 186801 (2014).

[29] G. Martinez, Band inversion in Pb$_{1-x}$Sn$_x$Se alloys under hydrostatic pressure. II. Galvanomagnetic properties, Phys. Rev. B **8**, 4686 (1973).

[30] G. Krizman, B. A. Assaf, T. Phuphachong, G. Bauer, G. Springholz, L. A. de Vaulchier, and Y. Guldner, Dirac parameters and topological phase diagram of Pb$_{1-x}$Sn$_x$Se from magnetospectroscopy, Phys. Rev. B **98**, 245202 (2018).

[31] B. A. Assaf, T. Phuphachong, V. V Volobuev, G. Bauer, G. Springholz, L.-A. De Vaulchier, and Y. Guldner, Magnetooptical determination of a topological index, Npj Quantum Mater. **2**, 26 (2017).

[32] M. Simma, G. Bauer, and G. Springholz, Band alignments and strain effects in PbTe/Pb$_{1-x}$Sr$_x$Te and PbSe/Pb$_{1-x}$Sr$_x$Se

quantum-well heterostructures, Phys. Rev. B **90**, 195310 (2014).

[33] M. Simma, G. Bauer, and G. Springholz, Temperature dependent band offsets in PbSe/PbEuSe quantum well heterostructures, Appl. Phys. Lett. **101**, 172106 (2012).

[34] E. Bangert, G. Bauer, E. J. Fantner, and H. Pascher, Magneto-optical investigations of phase-transition-induced band-structure changes of $Pb_{1-x}Ge_x$Te, Phys. Rev. B **31**, 7958 (1985).

[35] A. Lau and C. Ortix, Topological Semimetals in the SnTe Material Class: Nodal Lines and Weyl Points, Phys. Rev. Lett. **122**, 186801 (2019).

[36] J. Liu, C. Fang, and L. Fu, Tunable Weyl fermions and Fermi arcs in magnetized topological crystalline insulators, Chin. Phys. B **28**, 047301 (2019).

[37] G. Bauer, H. Pascher, and W. Zawadzki, Magneto-optical properties of semimagnetic lead chalcogenides, Semicond. Sci. Technol. **7**, 703 (1992).

[38] G. Springholz, Molecular beam epitaxy of IV-VI semiconductors: Fundamentals, low dimensional structures, and device applications, in *Molecular Beam Epitaxy: From Research to Mass Production*, 2nd ed. (Elsevier Science Publishing Co., Oxford, 2018).

[39] Y. Ando and L. Fu, Topological crystalline insulators and topological superconductors: from concepts to materials, Annu. Rev. Condens. Matter Phys. **6**, 361 (2015).

[40] H.-Z. Lu, W.-Y. Shan, W. Yao, Q. Niu, and S.-Q. Shen, Massive Dirac fermions and spin physics in an ultrathin film of topological insulator, Phys. Rev. B **81**, 115407 (2010).

[41] R. Buczko and Ł. Cywiński, PbTe/PbSnTe heterostructures as analogs of topological insulators, Phys. Rev. B **85**, 205319 (2012).

[42] G. Bastard, *Wave Mechanics Applied to Semiconductor Heterostructures* (Les Editions de Physique, Les Ulis, France, 1988).

[43] G. Bastard, Superlattice band structure in the envelope-function approximation, Phys. Rev. B **24**, 5693 (1981).

[44] G. Bastard, Theoretical investigations of superlattice band structure in the envelope-function approximation, Phys. Rev. B **25**, 7584 (1982).

[45] Y.-C. Chang, J. N. Schulman, G. Bastard, Y. Guldner, and M. Voos, Effects of quasi-interface states in HgTe-CdTe superlattices, Phys. Rev. B **31**, 2557 (1985).

[46] D. L. Mitchell and R. F. Wallis, Theoretical energy-band parameters for the lead salts, Phys. Rev. **151**, 581 (1966).

[47] E. A. de Andrada e Silva, Optical transition energies for lead-salt semiconductor quantum wells, Phys. Rev. B **60**, 8859 (1999).

[48] A. C. Bartnik, A. L. Efros, W.-K. Koh, C. B. Murray, and F. W. Wise, Electronic states and optical properties of PbSe nanorods and nanowires, Phys. Rev. B **82**, 195313 (2010).

[49] P. Rothlein, H. Pascher, G. Bauer, and M. Tacke, Coherent Raman scattering and magneto-optical interband transitions in diluted magnetic IV-VI compounds, Semicond. Sci. Technol. **5**, S147 (1990).

[50] S. Tchoumakov, V. Jouffrey, A. Inhofer, E. Bocquillon, B. Plaçais, D. Carpentier, and M. O. Goerbig, Volkov-Pankratov states in topological heterojunctions, Phys. Rev. B **96**, 201302(R) (2017).

[51] X. Lu and M. O. Goerbig, Dirac quantum well engineering on the surface of a topological insulator, Phys. Rev. B **102**, 155311 (2020).

[52] B. A. Assaf, T. Phuphachong, V. V Volobuev, A. Inhofer, G. Bauer, G. Springholz, L. A. de Vaulchier, and Y. Guldner, Massive and massless Dirac fermions in $Pb_{1-x}Sn_x$Te topological crystalline insulator probed by magneto-optical absorption, Sci. Rep. **6**, 20323 (2016).

[53] See Supplemental Material at http://link.aps.org/supplemental/10.1103/PhysRevB.103.235302 for all the band parameters determined from experiments and calculations of the miniband dispersions in the vicinity of the topological phase transition and of higher order states.

[54] Z.-Y. Ye, H.-X. Deng, H.-Z. Wu, S.-S. Li, S.-H. Wei, and J.-W. Luo, The origin of electronic band structure anomaly in topological crystalline insulator group-IV tellurides, Npj Comput. Mater. **1**, 15001 (2015).

[55] T. Story, R. R. Gałazka, R. B. Frankel, and P. A. Wolff, Carrier-Concentration Induced Ferromagnetism in PbSnMnTe, Phys. Rev. Lett. **56**, 777 (1986).

[56] L. Kowalczyk, Determination of the exchange interaction parameters from interband magnetoemission in $Pb_{1-x}Mn_x$Se, Semicond. Sci. Technol. **6**, 115 (1991).

[57] T. Dietl, C. Śliwa, G. Bauer, and H. Pascher, Mechanisms of exchange interactions between carriers and Mn or Eu spins in lead chalcogenides, Phys. Rev. B **49**, 2230(R) (1994).

[58] J. O. Dimmock, $k \cdot p$ theory for the conduction and valence bands of PbSnTe and PbSnSe alloys, in *Proceedings of the International Conference of the Physics of Semimetals and Narrow Gap Semiconductor* (1971), pp. 319–330.

[59] G. Bauer, Magnetooptical properties of IV–VI compounds, *Narrow Gap Semicond. Phys. Appl. Proc. Int. Summer Sch.*, edited by W. Zawadzki, Lecture Notes in Physics Vol. 133 (Springer, Berlin, 1980), p. 427.

[60] G. Krizman, B. A. Assaf, M. Orlita, G. Bauer, G. Springholz, R. Ferreira, L. A. de Vaulchier, and Y. Guldner, Interaction between interface and massive states in multivalley topological heterostructures (unpublished).